Numerical simulations of single-mode Richtmyer-Meshkov experiments

Claude Mügler* and Serge Gauthier
Commissariat à l'Energie Atomique, Bruyères-le-Châtel, Boîte Postale 12, 91680 Bruyères-le-Châtel, France
(Received 23 February 1998)

Two-dimensional numerical simulation of the fluid instability of a shock-accelerated interface between a light fluid and a heavy one shows a flow pattern very similar to experimental pictures. Furthermore, numerical and experimental amplitude growth rates are in good agreement and are decaying in time in a similar way. Spectral analysis of the flow is performed with the help of two different methods. The peak-to-peak amplitude can be reproduced with 50 mesh zones in the wavelength whereas the streamwise kinetic energy decay in time due to molecular viscous dissipation requires 360 zones in the wavelength and a second-order accurate numerical scheme in space and time to be correctly described. [S1063-651X(98)04410-9]

PACS number(s): 47.20.−k, 47.40.Nm

I. INTRODUCTION

When two different fluids are impulsively accelerated into each other by a shock wave, small perturbations at the interface grow first linearly and then evolve into nonlinear structures having the form of ''bubbles'' and ''spikes.'' This instability was theoretically discovered and described by Richtmyer [1], and confirmed experimentally by Meshkov [2]. This phenomenon, known as the Richtmyer-Meshkov (RM) instability, is a typical mechanism for turbulent mixing of layered fluids. It may be related to the Rayleigh-Taylor (RT) instability [3], which is the instability of a planar interface undergoing constant acceleration, such as caused by the suspension of a heavy fluid over a lighter one in the earth's gravitational field. RT and RM instabilities are of critical importance to inertial confinement fusion. Indeed, the degree of compression achievable in laser fusion experiments is ultimately limited by RM and RT instabilities.

RM instability is often studied in shock tubes, where measurements are easier to carry out than in small pellets [4–8]. The major difficulty in shock-tube experiments is in maintaining a well-controlled sharp initial boundary between two gases. One solution to this problem is to initially separate the two gases using a thin membrane. The membrane has little strength and is expected to rupture upon passage of the first shock, although this is not always the case [4,5]. To impose the membrane rupture, discontinuous interfaces are sometimes made of a plastic membrane that is placed directly below a thin wire mesh [5,6]. The membrane is broken into small pieces by the incident shock wave passing through the grid. Other shock-tube experiments have attempted to avoid the effects of membranes by implementing systems in which gases are initially separated by a solid barrier, which is removed just prior to firing the shock tube [8,9]. However, this technique generates relatively thick diffuse interfaces. The diffuse interface tends to stabilize all but the longest wavelengths, thus greatly reducing the resulting instability growth rate.

A number of numerical studies have been performed on the RM instability [10,11]. The initial growth rate of the perturbation, which is measured between the first and second shocks across the interface, was predicted in two-dimensional calculations to be approximately a factor of 2 too large, as compared with experimental data [10,12]. More recently, front-tracking numerical simulations produced growth rates in much closer agreement to the experimental values [13].

The present study uses the experimental conditions of Zaytsev and co-workers [14,15], who performed shock tube experiments of krypton incident on xenon. In these experiments, a very thin membrane separates the two gases and provides a known initial interface perturbation. The experimental images show well-resolved flow patterns, but do not lead to other flow characteristics. In this paper, we simulate the nonlinear instability growth observed in the experiments. In the next two sections, we present experimental and numerical results. Finally, these results are discussed in Sec. IV.

II. EXPERIMENTS

The experimental study of a two-dimensional RM instability has been carried out in a shock tube of square cross section of $72\times 72\ \mathrm{mm}^2$ [15]. At about 4.5 m from the diaphragm separating the high- from the low-pressure rooms of the shock tube, two inert gases, a light one (krypton) and a heavy one (xenon), are initially separated by a two-dimensional (2D) sinusoidal interface. This interface is modeled with a 2-μm-thick lavsan film. This film is pasted into a matrix inserted in the driven section. The study of the shock wave interaction with the 2D film has shown that the film does not affect the interface evolution [14]. Just before each experiment, both parts of the driven section are pumped out to 0.01 mm Hg and then filled with test gases. The diagnostics used during these experiments are some schlieren pictures. A detailed description of the setup can be found in Ref. [14].

The initial amplitude of the perturbation at the Kr/Xe interface is $a_0^- = 5\ \mathrm{mm}$, the wavelength is 36 mm, and the pressure ahead of the shock is 0.5 bar. The Kr/Xe interface is accelerated by a 3.5-Mach number shock wave moving from Kr to Xe, i.e., from a light gas to a heavy one. The reflected wave is a shock wave. To observe the evolution of the insta-

*Electronic address: mugler@bruyeres.cea.fr

bility on a sufficiently long time scale, three experimental shots have been necessary. The Mach number is not exactly the same for the three experiments but does not differ too much from 3.5.

III. NUMERICAL METHOD

A. Motivation and description of the numerical choices

The code CADMEE, derived from CFDLIB [16], was developed in order to carry out two-dimensional numerical simulations of compressible mixing flows, such as those occurring in shock tubes. Features of the numerical method are detailed in Ref. [17] but let us recall here the main characteristics of the code CADMEE: (i) It solves the 2D unsteady full Navier-Stokes equations, with physical viscosity and thermal conductivity coefficients. (ii) Mixing of two gases is described within the single fluid approximation by a concentration governed by an advection-diffusion equation, written as

$$\frac{\partial \rho c}{\partial t}+\vec{\nabla}\cdot(\rho \vec{u} c)=\vec{\nabla}\cdot(\rho D \vec{\nabla} c), \tag{1}$$

where ρ is the total density and $\vec{u}$ the vector velocity. Partial densities of fluids 1 and 2, ρ_1 and ρ_2, respectively, and the total density ρ are related by the equation $\rho=\rho_1+\rho_2$. The concentration of fluid 1 in the mixing, labeled c, is defined as the ratio ρ_1/ρ. By doing so, no numerical interface and no mixed cells are needed. (iii) Mixing is assumed perfect and isothermal. The mixing model is then simply defined by $P=P_1+P_2$, $T=T_1=T_2$, and $e=ce_1+(1-c)e_2$, where ρ, P, and e are the total density, pressure, and internal energy, respectively. The indices refer to the partial corresponding quantities of fluids 1 and 2. The equation of state of each species is a perfect gas law. (iv) The viscosity and molecular diffusion coefficients of each species of the mixture are calculated from Ref. [18]. Thermal conductivity coefficients can be obtained directly from viscosity coefficients provided the Prandtl number of each species is assumed to be constant. Mixture viscosity and molecular diffusion coefficients are then determined from Wilke's mixture rule [19] and the thermal conductivity coefficient of the mixture is calculated from the model given in [20]. Finally, all transport coefficients (viscosity, diffusion, and thermal conductivity) depend on the two thermodynamic quantities: concentration and temperature. (v) CADMEE uses structured meshes made of quadrangular cells. (vi) State variables are cell centered. (vii) A Godunov method is used to accurately describe strong discontinuities such as shock waves. It uses the approximate Riemann solver of Dukowicz [21]. Consequently, no artificial viscosities are needed. (viii) A second-order differencing technique in space can be used and second and third Runge-Kutta schemes (RK2 and RK3) have been implemented. We shall see in the following sections the influence of the accuracy of numerical methods. (ix) The computation is performed in two phases: a Lagrangian phase and a remapping phase in which conservative variables are transferred from the Lagrangian mesh to an arbitrary specified mesh. This approach is the so-called arbitrary Lagrangian-Eulerian (ALE) formulation.

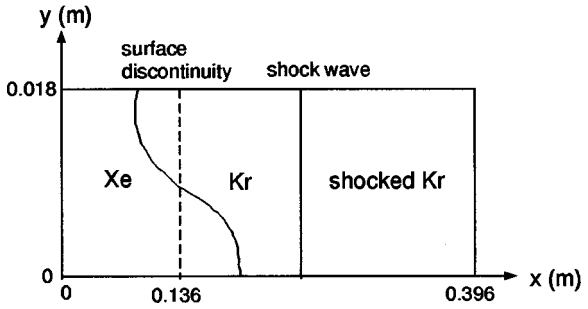

FIG. 1. Shock-tube geometry.

The code CADMEE has been validated against numerous configurations of compressible viscous flows [17].

B. Results of numerical simulations

In this subsection, we will first study the influence of spatial resolution and of the order of the temporal and spatial schemes on numerical results. The definition of the initial hydrodynamic conditions is based on shock-tube experiments previously described. The shock tube can be idealized by considering a long tube as presented in Fig. 1. The mesh extends from $x=0$ to 39.6 cm along the length of the shock tube and covers a quarter of the width of the square cross section. Although mixing is described by a concentration, at $t=0$, the concentration isovalue $c=0.5$ can be seen as a sharp interface. At later times, the mixing zone between krypton and xenon remains very thin. So, we will still use the word ''interface.'' The initial sinusoidal 2D interface between krypton and xenon is given by

$$x_{\text{interface}}=x_m+a_0^- \cos\frac{2\pi y}{\lambda}, \tag{2}$$

where $x_m=13.6$ cm is the location of this interface, $a_0^-=5$ mm the initial amplitude of the perturbation, and $\lambda=3.6$ cm its wavelength. The dimensionless perturbation amplitude $a_0^- k$ is 0.87. The region to the left of the interface contains xenon while the region to the right contains krypton. The shock wave is initially in the krypton at $x=14.8$ cm and is moving to the left at Mach number $M=3.5$. The fluid velocity behind the shock is -55.5 m/s. The shocked krypton has a density of 6.01 kg/m^3, a pressure of 75.3×10^4 Pa, and a ratio of specific heats $\gamma=1.67$. The unshocked krypton has a density of 1.87 kg/m^3 and a pressure of 5.0×10^4 Pa. The unshocked xenon has a density of 2.95 kg/m^3, a pressure of 5.0×10^4 Pa, and a ratio of specific heats $\gamma=1.67$. An ideal gas equation of state with constant specific heats is assumed. With such initial conditions, the interface is nearly stationary after shocking and is confined to the region 13 cm$\leqslant x\leqslant$14 cm and $0\leqslant y\leqslant$18 cm, which we cover with square zones. The region from $x=14$ cm to $x=39.6$ cm is used only to contain the reflected shock in such a way that no spurious numerical signal is reflected into the mixing region.

The instant $t=0$ corresponds to the moment the shock strikes the right edge of the perturbation. The right and left boundaries are of flow through type. In this part, only a half-wavelength is simulated and the top and bottom bound-

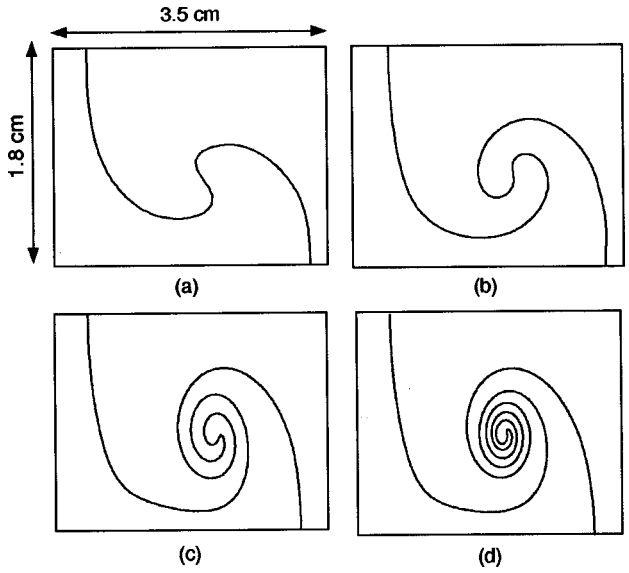

FIG. 2. Isovalue of the concentration $c=0.5$ for various grids: (a) cell size$=0.75\times0.72$ mm^2, (b) cell size$=0.375\times0.36$ mm^2, (c) cell size$=0.1875\times0.18$ mm^2, (d) cell size$=0.1\times0.1$ mm^2. The numerical scheme is second order accurate in space and time.

aries are free-slip boundaries. The calculation is started with a Lagrangian mesh with nodes located at the initial interface, and continued with a Eulerian grid before the shock reaches the interface. By doing so, the development of undesired perturbations of wavelengths of the order of the mesh size is avoided.

Several runs were carried out with various zone sizes 0.75×0.72 mm^2, 0.375×0.36 mm^2, 0.1875×0.18 mm^2, and 0.1×0.1 mm^2, and with a Courant-Friedrichs-Lewy number equal to 0.9. Such resolutions correspond to 50, 100, 200, and 360 zones in the wavelength, respectively. These calculations have been performed with the second-order scheme in space and time. Figure 2 shows the isovalue of the concentration $c=0.5$ at $t=1$ ms for each of these four zone sizes. The sizes of the window are 3.5 cm width and 1.8 cm height for all figures in this paragraph. At a zone size of 0.75×0.72 mm^2 [Fig. 2(a)], the mushroom develops but the Kelvin-Helmholtz instability along the shaft of each spike needs a thinner grid to be well described [Figs. 2(b), 2(c), and 2(d)]. The thinner the grid, the greater the number of rolling-ups.

For a fixed grid, we also studied the influence of the spatial and temporal accuracy of the numerical scheme on the development of the instability (see Fig. 3). This study was

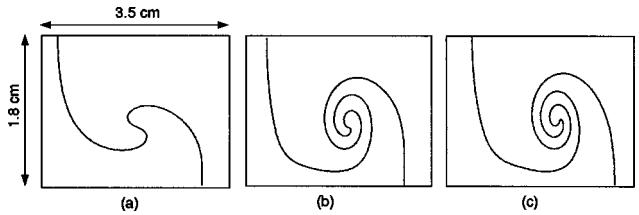

FIG. 3. Isovalue of the concentration $c=0.5$ for various spatial and temporal accuracy, with a fixed grid cell size$=0.1875\times0.18$ mm^2: (a) first-order accuracy in space and time, (b) second order in space, first order in time, (c) second order in space and time.

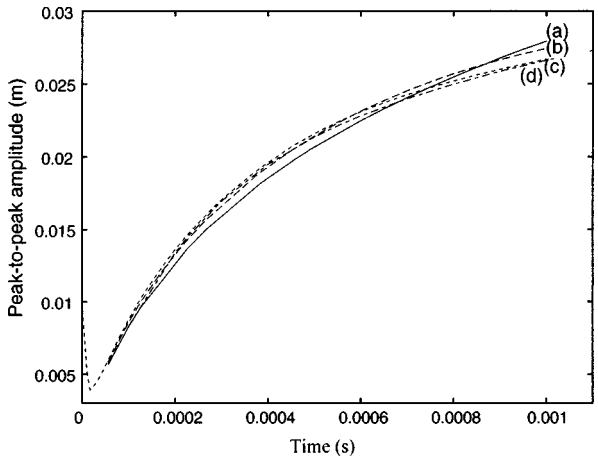

FIG. 4. Evolution of the perturbation amplitude vs time. This amplitude is defined as the peak-to-peak amplitude of the isovalue $c=0.5$ obtained from various grids: (a) cell size$=0.75\times0.72$ mm^2, (b) cell size$=0.375\times0.36$ mm^2, (c) cell size$=0.1875\times0.18$ mm^2, (d) cell size$=0.1\times0.1$ mm^2.

carried out with a zone size of 0.1875×0.18 mm^2. With a first-order method in space and in time [Fig. 3(a)], the numerical scheme is too diffusive and prevents the Kelvin-Helmholtz instability development. With a second-order method in space and first order in time [Fig. 3(b)], the flow pattern has completely changed and the Kelvin-Helmholtz vortex has appeared. However, temporal accuracy effects are less spectacular than spatial accuracy ones: with a second-order method in space, the increase of the accuracy in time (use of RK2) induces only small differences [Fig. 3(c)]. Moreover, we have checked to be sure that a higher-order scheme in time such as a third Runge-Kutta scheme does not bring any significant improvement. These results illustrate the importance of the accuracy of numerical methods and of spatial resolution.

From the four calculations performed with various zone sizes, we can measure and plot the evolution of the perturbation amplitude versus time (see Fig. 4). This amplitude is defined as the peak-to-peak amplitude of the concentration isovalue $c=0.5$. The discrepancies between the various curves are less than the cell sizes. We can conclude that the peak-to-peak amplitude is converged in terms of zone sizes. However, the flow pattern, as shown in Fig. 3, is not converged. Indeed, Kelvin-Helmholtz instability is very sensitive to the shock description through the baroclinic term in the vorticity equation. The thinner the grid, the stiffer the shock, the more developed the Kelvin-Helmholtz instability. Convergence would require zone sizes smaller than the physical shock thickness. Such zone sizes are two or three orders of magnitude smaller than those used in this paper. In the next section, if it is not explicitly mentioned, numerical results correspond to calculations performed with a zone size of 0.1875×0.18 mm^2.

IV. COMPARISONS AND DISCUSSIONS

Schlieren pictures of the RM instability evolution at the Kr/Xe interface are presented in Fig. 5. These results correspond to the three experimental shots presented in Sec. II. As the incident shock wave travels from the light gas to the

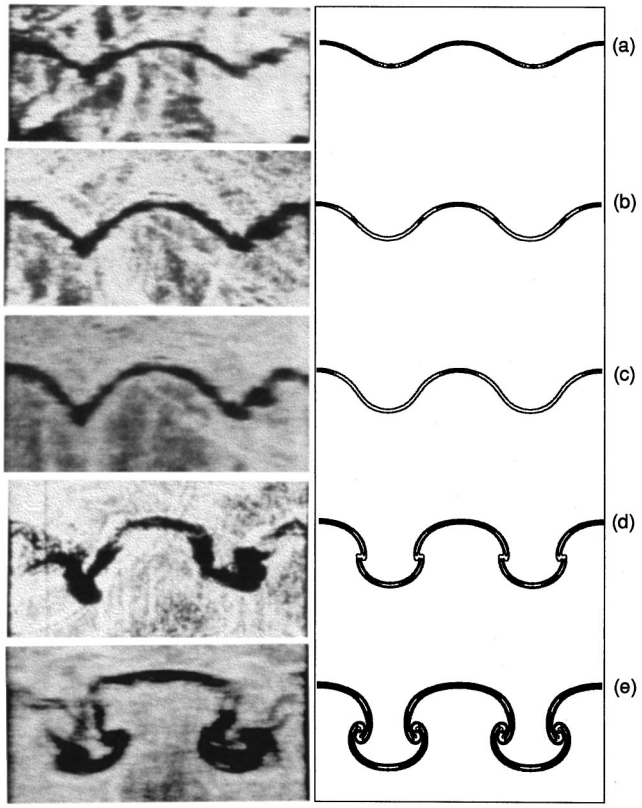

FIG. 5. Evolution of the flow pattern vs time: experimental schlieren pictures of the RM instability (left) and numerical schlieren-type images with $\alpha=2$ in Eq. (3) (right). (a)–(e) are for $t=0$, 65, 108, 134, 276, and 464 μs, respectively.

heavy one, there is no inversion of concavity after the shock passage. As one can see in these pictures, the perturbation amplitude grows first linearly and then in a nonlinear stage. There is apparition of structures called ''bubbles'' and ''spikes'': the heavy fluid penetrates in the light fluid. As the Atwood number is small ($A=0.22$ and $A=0.184$ before and after the passage of the incident shock wave) the difference of structure between bubbles and spikes is not important and the Kelvin-Helmholtz instability is well developed. In the above, the Atwood number is defined as $(\rho_2-\rho_1)/(\rho_2+\rho_1)$, where ρ_1 is the density of the first shocked fluid.

Figure 5 also shows the time evolution of the numerical patterns obtained from schlieren-type images. As the magnitude of the gradient of the density field near a shock wave is very large, the following nonlinear shading function Φ is used to accentuate weak flow features in numerical images:

$$\Phi=1-\exp\left(-\alpha\,\frac{|\vec{\nabla}\rho|}{|\vec{\nabla}\rho|_{\max}}\right), \tag{3}$$

where α is a constant (see, for example, Ref. [22]). As shown in Fig. 5, the visual agreement between experimental schlieren pictures and numerical schlieren-type images is good. Such numerical images are particularly useful to simultaneously visualize interface and shock structures. As an example, Fig. 6 gives the full numerical schlieren-type image of the flow at $t=108$ μs. It shows locations and structures of the interface and of the refracted and reflected shock on the Kr/Xe interface. The distortion of the reflected shock due to its reflection on the perturbed interface clearly appears. We can also observe crisscross lines between the Kr/Xe interface and the reflected shock wave. Indeed, at the end of the interaction between the incident shock wave and the Kr/Xe interface, the curved refracted and reflected shock waves generate local high-pressure areas. Zaytsev *et al.* [14] have experimentally shown that once the high-pressure regions have appeared, they start ''outspreading.'' For sufficiently high values of the pressure amplitude in these regions, this outspreading is accompanied by the generation of secondary shock waves. In Fig. 6, two secondary shock waves traveling behind the perturbed reflected shock wave have just interacted. We have verified that after traveling a certain distance, the reflected shock wave becomes nearly flat. The numerous shock interactions result in changes in density and velocity. For example, in Fig. 6, close to the Kr/Xe interface, very low density variations of the order of 3% can be seen on the schlieren-type image obtained with $\alpha=10$ in Eq. (3) because, with such a value of α, this diagnostic is very sensitive. On the other hand, they do not appear on schlieren-type images obtained with $\alpha=2$ (see Fig. 5).

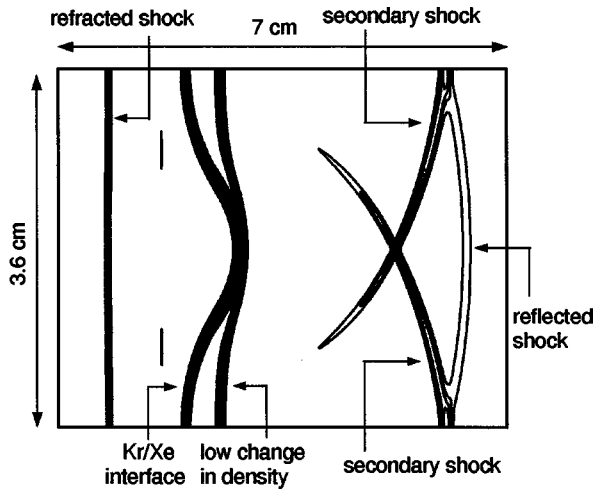

FIG. 6. Full numerical schlieren-type image at $t=108$ μs, with $\alpha=10$ in Eq. (3). The distortion of the shock reflected on the Kr/Xe interface clearly appears.

From experimental schlieren pictures, the interface and the refracted shock locations and the perturbation height are measured at various times. In order to compare experiments with calculations on a quantitative way, we have plotted the perturbation height time evolution. In experiments, the perturbation height is defined as the longitudinal distance between the spike and bubble tips. In numerical simulations, this height is defined as the largest distance between the isovalues of the concentration $c=5\%$ and $c=95\%$. Experimental and numerical results are plotted in Fig. 7(a). Error bars of experimental data are equal to $\pm 5\%$. As we can see, the perturbation height in the simulation is approximately the same as in experimental pictures. We have also plotted in Fig. 7(b) the growth rate of the perturbation as obtained from experiments and numerical simulations. As can be seen from this figure, numerical simulation results are in agreement with experimental data even in the nonlinear regime. The growth rate of the perturbation, dL/dt, can be used to calculate the Mach number of the perturbation, defined as $(dL/dt)/c_s$ where c_s is an average of the sound speeds in

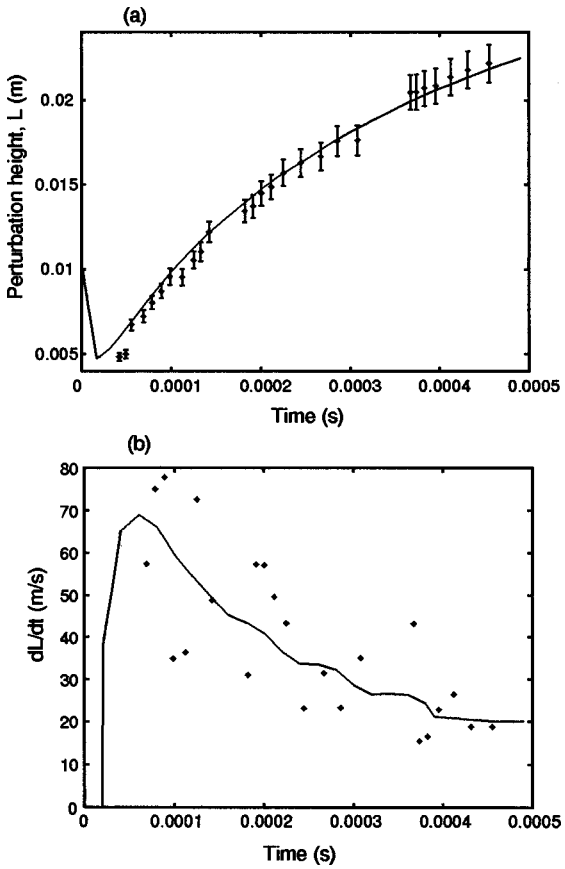

FIG. 7. Evolution of the perturbation height and perturbation growth rate vs time. Plots correspond to experimental data. The error bars are equal to ±5%. Full lines correspond to numerical results obtained from code CADMEE.

krypton and xenon. This Mach number rapidly decreases versus time, from the value of 0.16 just after the shock passage, down to 0.04. We also noticed that the maximum value of the velocity divergence is always five orders of magnitude smaller than the maximum value of the vorticity. These results show that the RM unstable system rapidly evolves to a vortical dominated flow.

The impulsive model first proposed by Richtmyer [1] is commonly used to estimate the growth rate of a shock accelerated interface in the linear phase. However, a new general formula for the growth rate of the Richtmyer-Meshkov instability has been recently derived within the framework of the impulsive model [23,24]. This formula, which allows us to predict the growth rate in both configurations (heavy-light and light-heavy configurations) has been validated over more than one hundred cases with various values of both the shock strength parameter ϵ and the adiabatic exponents. It produces a good estimate of the growth rate of the RM instability provided it is used within its range of validity, i.e., $\epsilon \leqslant 0.4$ and a ratio of adiabatic exponents less than 1.5. In the experiments simulated in this paper, the shock strength parameter ϵ is equal to 0.93 and the dimensionless perturbation amplitude $a(0^-)k$ is equal to 0.87. As a result, a compressible and nonlinear theory is needed and the formulas [1,23,24] can no longer be used. A quantitative nonlinear theory of compressible Richtmyer-Meshkov instability has recently been developed [25]. It gives predictions in good agreement with the results of full numerical simulations from linear to nonlinear regimes.

The nonlinear evolution of the perturbation has been studied by two different methods of modal analysis. In the first spectral analysis, we isolate the concentration isovalue $c = 0.5$ and take its discrete Fourier transform. This first procedure gives an accurate representation of the interface at small times but it is no more valid when the ''interface'' becomes distorted and multivalued by the development of ''bubble'' and ''spike'' structures. So, a second spectral analysis has been developed. To this end, we introduce the new variable $w \equiv \sqrt{\rho} u$ where ρ is the density and u the streamwise velocity component, and we consider the one-dimensional transversal spectrum as done in Ref. [26],

$$E(k_y,t) = \frac{1}{2L_x} \int_{-L_x}^{+L_x} |\hat{w}(x,k_y,t)|^2 dx. \tag{4}$$

In this expression, $\hat{w}(x,k_y,t)$ is the longitudinal discrete Fourier transform of the variable w at a given abscissa x,

$$\hat{w}(x,k_y,t) \equiv \hat{w}\left(x, \frac{l}{N\Delta y}, t\right) = \frac{1}{N} \sum_{j=0}^{N-1} w(x,j\Delta y,t) \exp\left(-i \frac{2\pi l j}{N}\right), \tag{5}$$

where $l = 0,1,...,N-1$, N is the number of samples, and Δy the sample interval. The length $2L_x \leqslant d$ corresponds to an x span on which the transversal spectrum is averaged. We will commonly choose d equal to the shock-tube square section and the length $2L_x$ greater than or equal to the perturbation height at the final time. The advantage of this second spectral analysis is to give information on all scales present in the mixing zone, even if the flow develops into a turbulent regime. Moreover, the quantity obtained is homogeneous to an energy, but, as it is calculated from only one velocity component, it is not the total kinetic energy.

In Fig. 8, the first spectral analysis is used and the Fourier spectrum of the isovalue of the concentration $c = 0.5$ is displayed at four early increasing times. These times are the same as those used in Fig. 5 where we have plotted the corresponding physical space outline. In Fig. 8, the mode index $l = 1$ corresponds to the wavelength $\lambda = 3.6$ cm. Notice that even at early times the interface is no longer monomode. The shortness of the linear phase has been noticed on other calculations and with another numerical code [27]. Indeed, the simulation with a 2D Lagrangian code of a monomode Richtmyer-Meshkov instability with an incident shock wave at a Mach number equal to 1.3 also showed the early growth of the first harmonic of the principal mode [27]. This multimode behavior that shows the evolution of the amplitudes of the various modes versus time is more noticeable in Fig. 9. It seems that during the interaction, which occurs at $t = 0$, the incident shock wave excites the first harmonic that afterwards slowly increases versus time.

At later times, the flow enters into the nonlinear regime with the familiar asymmetry between bubble and spike regions (see Fig. 5). We can no longer use the Fourier spectrum of the isovalue of the concentration $c = 0.5$ and we now use the second spectral analysis. In this method, we calculate the one-dimensional transversal spectrum of the quantity w, given by Eq. (4) and Eq. (5). Figure 10 gives the evolution of

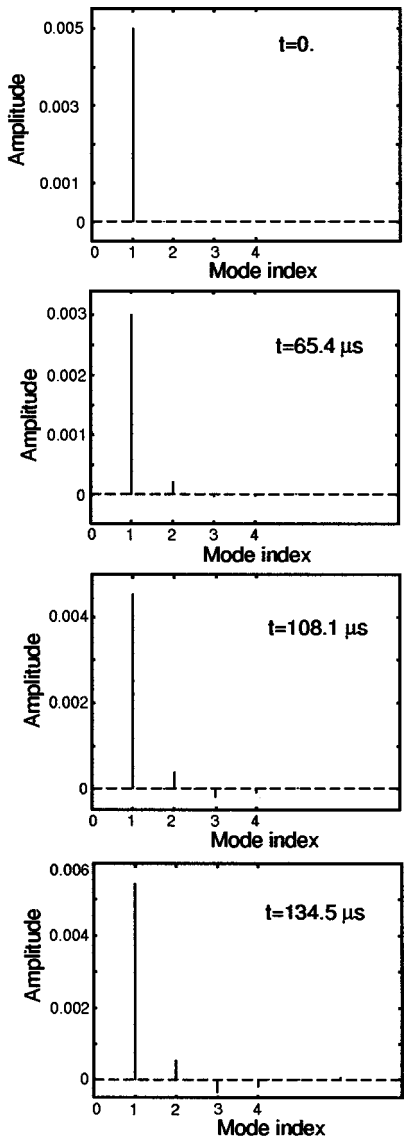

FIG. 8. Fourier transform of the concentration isovalue $c=0.5$ at four various times. At $t=0$, the interface is single mode. The mode index $l=1$ corresponds to the wavelength $\lambda=3.6$ cm.

the normalized amplitude $E(k_0)$ of the main mode k_0 versus time, with a ln scaling on the y axis. The three different symbols correspond to numerical simulations performed with three different spatial resolutions: a zone size of 0.375×0.36 mm^2 (diamonds in Fig. 10), a zone size of 0.1875×0.18 mm^2 (crosses) and a zone size of 0.1×0.1 mm^2 (squares). Such resolutions correspond to 100, 200, and 360 zones in the wavelength, respectively. In Fig. 10, the straight line gives the theoretical decay of the kinetic energy due to the viscous dissipation: its slope is equal to the product $-2\nu k_0^2$, where the physical kinematic viscosity ν is equal to 10^{-5} m^2/s. Once again, this figure clearly stresses the importance of spatial resolution on the streamwise kinetic energy decay: it needs a zone size of 0.1×0.1 mm^2, i.e., 360 zones in the wavelength, to recover an exponential energy decay equal to molecular viscous dissipation. This result shows that the one-dimensional transversal spectrum is very sensitive to the numerical resolution. At larger grids, the streamwise kinetic energy decay gives an estimate of numerical viscosity

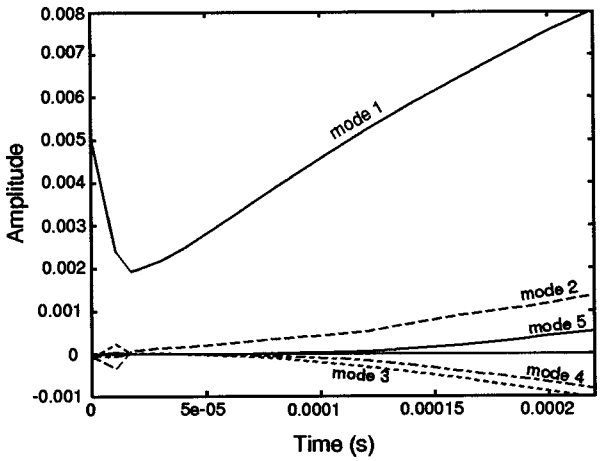

FIG. 9. Evolution of the amplitudes of the first five Fourier modes of the concentration isovalue $c=0.5$ vs time.

that becomes larger than molecular viscosity. The numerical viscosity ν_{num} is approximately 12 and 60 times larger than the physical kinematic viscosity ν at a resolution of 200 and 100 zones in the wavelength, respectively, if we assume that numerical dissipation is dominated by a Laplacian that is written in the spectral space as $-2\nu_{\text{num}}k^2$.

In order to verify that the exponential decay in time is really due to molecular viscous dissipation, we have performed two other numerical simulations with the thinnest spatial resolution and with greater values of the kinetic viscosity. Figure 11 gives the evolution of the normalized amplitude $E(k_0)$ of the main mode k_0 versus time, with a ln scaling on the y axis. The three different symbols correspond to numerical results obtained from three viscosity coefficient values: $\nu=1\times10^{-5}$ m^2/s (squares in Fig. 11), $\nu=12\times10^{-5}$ m^2/s (crosses), and $\nu=60\times10^{-5}$ m^2/s (diamonds).

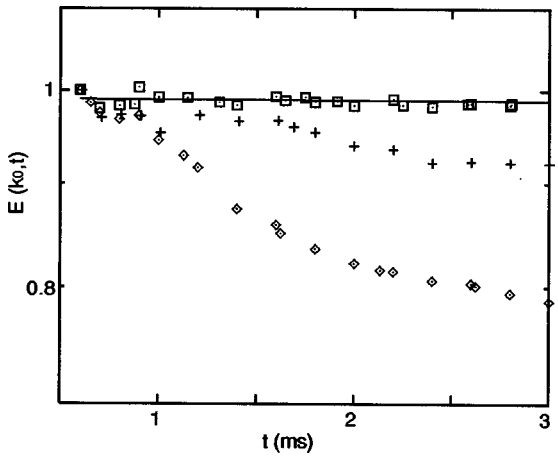

FIG. 10. Evolution of the normalized amplitude $E(k_0)$ of the main mode k_0 versus time, with a ln scaling on the y axis. The three different symbols correspond to numerical results obtained from three different zone sizes: 0.375×0.36 mm^2 (diamonds), 0.1875×0.18 mm^2 (crosses), and 0.1×0.1 mm^2 (squares). The straight line represents the kinetic energy decay due to the main viscous dissipation term; its slope is equal to $-2\nu k_0^2$, where the physical kinematic viscosity ν is equal to 10^{-5} m^2/s. This figure clearly shows the importance of spatial resolution on the streamwise kinetic energy decay.

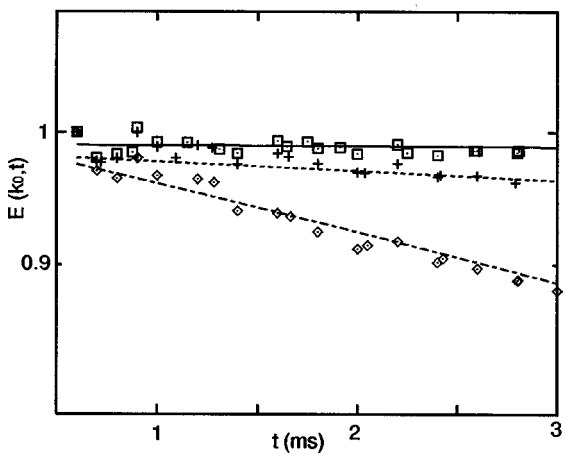

FIG. 11. Evolution of the normalized amplitude $E(k_0)$ of the main mode k_0 vs time, with a ln scaling on the y axis. The three different symbols correspond to numerical results obtained from three different viscosity coefficient values: $\nu=1\times10^{-5}$ m^2/s (squares), $\nu=1.2\times10^{-4}$ m^2/s (crosses), and $\nu=6\times10^{-4}$ m^2/s (diamonds). In each case, numerical results are well fitted with straight lines of slope $-2\nu k_0^2$ where ν is the corresponding value of the kinematic viscosity.

In each case, numerical results are well fitted with straight lines of slope $-2\nu k^2$ where ν is the corresponding value of the kinematic viscosity. We can conclude that the streamwise kinetic energy decays exponentially in time and that this decay is due to molecular viscous dissipation.

V. CONCLUSION

2D numerical simulations of the fluid instability of a shock-accelerated interface between a light fluid and a heavy one shows a flow pattern very similar to experimental pictures. Furthermore, numerical and experimental amplitude growth rates are in good agreement and are decaying in time in a similar way. On one hand, this comparison shows that it is possible to accurately simulate a RM instability provided the experimental initial conditions (amplitude and wave number of the 2D perturbation) are well known. On the other hand, this result allows us to conclude that the initial presence of the membrane at the interface, which is not simulated, has negligible effects on the development of the instability in this particular experiment. Simulations have been performed with the code CADMEE. In this numerical method, mixing is described by a concentration. This proves that front tracking is not necessary to obtain good agreement with experimental data.

At a sufficiently long time after the interaction between the shock wave and the interface, spectral analysis showed that the streamwise kinetic energy in the mixing zone decays exponentially in time. This exponential decay is clearly due to viscous dissipation. We have seen that we can recover the physical viscous dissipation behavior if we use a second accurate scheme in space and time and very high spatial resolution (360 zones in the wavelength). In such a case, physical viscous dissipation dominates numerical viscosity, which is not true with coarser grids. This result shows that higher-order numerical schemes would be welcome to accurately simulate Richtmyer-Meshkov experiments.

Spectral analysis also showed that the passage of an incident shock wave through an initially single-mode interface excites the main mode but also the first harmonic. Consequently, just after the interaction, the interface is no longer single mode. It is clear that there is still much to learn about the linear and nonlinear aspects of the Richtmyer-Meshkov instability to better understand how compressibility affects the fluid flow.

ACKNOWLEDGMENT

One of the authors (C.M.) is very grateful to Professor S. G. Zaytsev for useful discussions on his experiments.

[1] R. D. Richtmyer, Commun. Pure Appl. Math. **13**, 297 (1960).
[2] E. E. Meshkov, Fluid Dyn. (USSR) **4**, 101 (1969).
[3] G. I. Taylor, Proc. R. Soc. London, Ser. A **201**, 192 (1950).
[4] G. Rodriguez, I. Galametz, M.-H. Thorembey, C. Rayer, and J.-F. Haas, *Visualization of Shocked Mixing Zones Using Differential Interferometry and X-rays*, 20th International Symposium on Shock Waves, Pasadena, California, edited by H. Hornung (World Scientific, Singapore, 1996).
[5] M. Vetter and B. Sturtevant, Shock Waves **4**, 247 (1995).
[6] F. Poggi, M.-H. Thorembey, G. Rodriguez, and J.-F. Haas, in *Measurements of Velocity in the Turbulent Stage at Gaseous Mixtures Induced by Shock Waves*, IUTAM Symposium on Variable Density Low Speed Turbulent Flows, Marseille, edited by L. Fulachier, J. L. Lumley, and F. Anselmet (Kluwer Academic, Dordrecht, 1997).
[7] R. Bonazza and B. Sturtevant, Phys. Fluids **8**, 2496 (1996).
[8] I. Galametz, G. Delouis, M.-H. Thorembey, C. Rayer, G. Rodriguez, and J.-F. Haas, in *Visualization of Shocked Mixing Zones Using Differential Interferometry and X-rays*, Proceedings of the Fifth International Workshop on the Physics of Compressible Turbulent Mixing, edited by R. Young, J. Glimm, and B. Boston (World Scientific, Singapore, 1996).
[9] M. Brouillette and B. Sturtevant, J. Fluid Mech. **263**, 271 (1994).
[10] L. D. Cloutman and M. F. Wehner, Phys. Fluids A **4**, 1821 (1992).
[11] R. M. Baltrusaitis, M. L. Gittings, R. P. Weaver, R. F. Benjamin, and J. M. Budzinski, Phys. Fluids **8**, 2471 (1996).
[12] K. A. Meyer and P. J. Blewett, Phys. Fluids **15**, 753 (1972).
[13] J. W. Grove, R. Holmes, D. H. Sharp, Y. Yang, and Q. Zhang, Phys. Rev. Lett. **71**, 3473 (1993).
[14] S. G. Zaytsev, A. N. Aleshin, E. V. Lazareva, S. N. Titov, E. I. Chebotareva, V. Rozanov, I. Lebo, and V. Demchenko, in *Experimental Investigation of Rayleigh-Taylor and Richtmyer-Meshkov Instabilities*, edited by N. Wilke, Proceedings of the Third International Workshop on the Physics of Compressible Turbulent Mixing (CEA DAM Press, Paris, 1997).
[15] A. N. Aleshin, E. V. Lazareva, and S. G. Zaytsev (unpublished).

[16] F. L. Addesio, J. R. Baumgardner, J. K. Dukowicz, N. L. Johnson, B. A. Kashiva, R. M. Rauenzhan, and C. Zemach, in Los Alamos National Laboratory, Report No. 10613 (1990).
[17] C. Mügler, S. Gauthier, L. Hallo, and S. Aubert, AIAA Report No. 96-2068 (1996).
[18] J. O. Hirschfelder, C. F. Curtiss, and R. B. Bird, *Molecular Theory of Gases and Liquids* (Wiley, New York, 1954).
[19] C. R. Wilke, J. Chem. Phys. **18 (4)**, 517 (1950).
[20] E. A. Mason and S. C. Saxena, Phys. Fluids **1**, 361 (1958).
[21] J. K. Dukowicz, J. Comput. Phys. **61**, 119 (1985).
[22] J. J. Quirk and S. Karni, ICASE Report No. 94-75 (1994).
[23] C. Mügler, M. Vandenboomgaerde, and S. Gauthier, in *Richtmyer-Meshkov Instability in Inviscid and Viscous Flows*, Proceedings of the Fifth International Workshop on the Physics of Compressible Turbulent Mixing, edited by R. Young, J. Glimm, and B. Boston (World Scientific, Singapore, 1996).
[24] M. Vandenboomgaerde, C. Mügler, and S. Gauthier, *Richtmyer-Meshkov Instability: the Impulsive Model Revisited*, Proceedings of the Sixth International Workshop on the Physics of Compressible Turbulent Mixing, edited by G. Jourdan and L. Houas (Caractère, Marseille, 1997); see also Phys. Rev. E **58**, 1874 (1998).
[25] Q. Zhang and S. I. Sohn, Phys. Fluids **9**, 1106 (1997).
[26] M. Lesieur, C. Staquet, P. Le Roy, and P. Comte, J. Fluid Mech. **192**, 511 (1988).
[27] J.-M. Clarisse (private communication).